

See discussions, stats, and author profiles for this publication at: <https://www.researchgate.net/publication/362272959>

Geometry of deep and intermediate water breaking waves influenced by wind speed and direction

Article in *Physics of Fluids* · July 2022

DOI: 10.1063/5.0101943

CITATIONS

2

READS

157

2 authors:



Haifei Chen

University of New Mexico

14 PUBLICATIONS 221 CITATIONS

[SEE PROFILE](#)



Qingping Zou

Heriot-Watt University

139 PUBLICATIONS 2,793 CITATIONS

[SEE PROFILE](#)

Some of the authors of this publication are also working on these related projects:



Flow vegetation interaction [View project](#)



Coastal Morphodynamics [View project](#)

Geometry of deep and intermediate water breaking waves influenced by wind speed and direction

Cite as: Phys. Fluids **34**, 087126 (2022); <https://doi.org/10.1063/5.0101943>

Submitted: 05 June 2022 • Accepted: 25 July 2022 • Accepted Manuscript Online: 26 July 2022 •

Published Online: 25 August 2022

Published open access through an agreement with Heriot-Watt University Institute for Infrastructure and Environment

 Haifei Chen (陈海飞) and  Qingping Zou (邹青萍)



View Online



Export Citation



CrossMark

ARTICLES YOU MAY BE INTERESTED IN

[Wave breaking probabilities under wind forcing in open sea and laboratory](#)

Physics of Fluids **34**, 032122 (2022); <https://doi.org/10.1063/5.0084276>

[Lattice Boltzmann model for simulation of flow in intracranial aneurysms considering non-Newtonian effects](#)

Physics of Fluids **34**, 073105 (2022); <https://doi.org/10.1063/5.0098383>

[Eulerian and Lagrangian transport by shallow-water breaking waves](#)

Physics of Fluids **34**, 032116 (2022); <https://doi.org/10.1063/5.0086434>

APL Machine Learning

Open, quality research for the networking communities

Now Open for Submissions

[LEARN MORE](#)



Geometry of deep and intermediate water breaking waves influenced by wind speed and direction

Cite as: Phys. Fluids **34**, 087126 (2022); doi: 10.1063/5.0101943

Submitted: 5 June 2022 · Accepted: 25 July 2022 ·

Published Online: 25 August 2022



View Online



Export Citation



CrossMark

Haifei Chen (陈海飞),^{1,2} and Qingping Zou (邹青萍)^{3,a)}

AFFILIATIONS

¹Department of Civil and Environmental Engineering, University of Maine, Orono, Maine 04469, USA

²Interdisciplinary Science Cooperative, University of New Mexico, Albuquerque, New Mexico 87131, USA

³The Lyell Centre for Earth and Marine Science and Technology, Institute for Infrastructure and Environment, Heriot-Watt University, Edinburgh, United Kingdom

^{a)}Author to whom correspondence should be addressed: q.zou@hw.ac.uk

ABSTRACT

Wind effects on the evolution of a breaking wave group due to dispersive focusing are investigated using a two-phase flow Navier–Stokes solver. The Navier–Stokes equations are solved for both air and water, with the air–water interface captured by the Volume of Fluid method and the turbulence by the Smagorinsky subgrid-scale stress model. The two-phase model is first validated with the experimental measurements with and without following wind action. The following wind delays the breaking and shifts the breaking location downstream, and vice versa for the opposing wind. The wind-induced drift current is mainly responsible for these shifts of breaking time and location. The shift of breaking location and time is approximately linearly proportional to the wind speed (wind induced drift current) under weak winds, but the shift saturates under strong winds. The direct wind forcing, on the other hand, plays an increasingly larger role in the wave breaking process in the presence of stronger wind. It was found that the strong following wind forcing enhances the initiation of wave breaking, while the strong opposing wind forcing may change breaking type or suppress wave breaking of large intensity, such as plunging breaking. Accordingly, the wave shape at breaking onset is altered considerably under strong winds. The following wind increases the maximum wave height and wave skewness slightly. However, the opposing wind may also increase the maximum wave height initially because of the wind drift current induced upwave refocusing of the wave group. Eventually, stronger opposing wind decreases the wave height and wave skewness.

© 2022 Author(s). All article content, except where otherwise noted, is licensed under a Creative Commons Attribution (CC BY) license (<http://creativecommons.org/licenses/by/4.0/>). <https://doi.org/10.1063/5.0101943>

I. INTRODUCTION

Wave breaking in deep water plays an important role in regulating the momentum, gas, and heat transport and fluxes across the air–sea interface. A better understanding of the wave-breaking process is required to improve the subgrid-scale parameterizations in ocean circulation models and coupled atmosphere–ocean simulations. Wave breaking is a strongly nonlinear intermittent two-phase flow process that dissipates wave energy through entraining air bubbles into the water and generates current, turbulence, and vortices of different types and scales. Wave breaking is regarded as the most important mechanism to dissipate wave energy and generate current and turbulence, yet it is not well understood. Lacking adequate parameterization of air–sea flux and breaking is one of the main reasons that wave forecasts often underestimate the peak wave during storms. Other consequences of

breaking include wave run-up, over-topping and slamming force, and damage to coastal and offshore structures, which are major engineering design concerns (Peregrine, 2003). As a result, breaking waves have received much attention. A few review papers specifically summarized the state-of-the-art research on breaking waves in deep and intermediate waters (Banner and Peregrine, 1993; Melville, 1996; Perlin *et al.*, 2013; Duncan, 2001; Kiger and Duncan, 2012) and breaking induced slamming forces on marine structures (Dias and Ghidaglia, 2018).

Determining the breaking onset, breaking wave geometry, and the breaking induced energy dissipation are critical to accurate wave modeling and reliable forecasts. It will also have a significant effect on the wave loading on coastal and ocean structures (Bullock *et al.*, 2007; Peregrine, 2003). Many studies have focused on breaking onset criteria and wave geometric properties of incipient wave breaking, such as

limiting steepness and breaking crest shape (Perlin *et al.*, 2013). Recently, Barthelemy *et al.* (2018) proposed an energy flux based unified breaking onset threshold for deep and intermediate depth water that may distinguish maximally tall non-breaking waves from marginally breaking waves in focusing wave groups. On the free surface, this threshold parameter is reduced to the ratio of water particle speed to wave crest speed. The local crest would undergo breaking if the threshold parameter is larger than $[0.85, 0.86]$. Wave geometry has been studied by a number of investigators in both deep water (Stansell *et al.*, 2003; Babanin *et al.*, 2010) and shallow water (Doering and Bowen, 1987; Peng *et al.*, 2009; Zou and Peng, 2011; Chella *et al.*, 2016, O'Dea *et al.*, 2021) with and without structures. The energy dissipation rate due to wave breaking is proportional to the fifth power of wave phase speed and the breaking strength parameter b (Phillips, 1985). The latter was found to be related to the bandwidth, the rate of focusing, and the shape of the breaking wave (Drazen *et al.*, 2008). By equating b with the maximum slope at breaking according to linear theory and combining it with a breaking threshold, Romero *et al.* (2012) achieved excellent agreement with existing laboratory data. The resulting b ranges over three orders of magnitude, applicable to both gently spilling and plunging breaking waves. Nonetheless, there is a lack of studies on wind influences on breaking wave geometry and wave energy dissipation, especially in the presence of opposing wind.

Wave breaking processes may be further complicated by the wind action (Reul *et al.*, 2008; Zou and Chen, 2017). However, the phenomenon of wind-modulated breaking of either short wind waves or long swell waves is not uncommon in the open ocean. Near the coast, the wind direction and speed strongly affect the breaker location and breaker type of the shoaling waves (Feddersen and Veron, 2005). Laboratory studies demonstrated that offshore winds cause the waves to break in shallower water closer to shore, and promote plunging, whereas onshore winds cause waves to break in deeper water farther from shore and promote spilling (Douglass, 1990; King and Baker, 1996; Jiang *et al.*, 2020; Sous *et al.*, 2021). These laboratory experiments (Feddersen and Veron 2005; Sous *et al.*, 2021) also demonstrated that onshore wind can change shoaling wave shape (i.e., skewness and asymmetry). The wave shape is a determining factor for the third-order velocity moments which are closely related to the wave-induced net sediment transport and sandbar migration (Roelvink and Stive, 1989; Crawford and Hay, 2001; Hoefel and Elgar, 2003; Hsu *et al.*, 2006; Ruessink *et al.*, 2012). Zdyrski and Feddersen (2020, 2021) proved theoretically that by acting through a wave-dependent surface pressure, wind can indeed change non-breaking wave shape through harmonic phase and relative harmonic amplitude in intermediate and deep water and that the changes become more pronounced in shallower water. Zdyrski and Feddersen (2022) studied the wind effects on shoaling solitary wave shape. The resulting wave profile was found to be approximately a superposition of a solitary wave, a shoaling-induced shelf, and a wind-induced, bound, dispersive, and decaying tail. There is a paucity of literature on how wind action changes the breaker location and type in the deeper ocean (Zou and Chen, 2017). The present study aims to examine the wind influences on a deep-water breaker in a dispersive focusing wave group.

Because of the inherent coupling between airflow and wave motion, many laboratory studies have been performed to examine the wind effect on the wave breaking process and airflow structures above the crest. Oh *et al.* (2005) studied the breaking criteria for wind waves and concluded

that the geometric and kinematic criteria were inadequate for predicting breaking onset and that the dynamic breaking criterion was more suitable for discriminating breaking waves in the presence of wind action. The study by Galchenko *et al.* (2012) suggests that wind forcing significantly reduces the energy loss in a single breaking event (breaking strength). Buckley and Veron (2016) measured the airflow structure above wind waves, which showed intermittent airflow separation behind the crest of steep/breaking waves, leading to the formation of a sheltered region downwind of the crest. Most other studies, however, investigated the breaking process of mechanically generated wave groups forced by the wind. Reul *et al.* (1999, 2008) observed that the instantaneous airflow separated from a breaking crest in a similar fashion to that occurs over a backward facing step. A correlation between the separation bubble size and the breaking crest geometry was established from this study. The crest-front steepness at incipient breaking is found to range from 0.15 to 0.30 (Fig. 2 in Reul *et al.*, 1999), and the critical surface slope downwind of the crest, above which airflow separates, is about 35° (Reul *et al.*, 2008). Touboul *et al.* (2006) and Kharif *et al.* (2008) found that the presence of wind action slightly increases the maximum wave height and delays the defocusing process of the dispersive wave group. They observed airflow separation at a surface slope smaller than 0.35 ($<20^\circ$). Their modeling results suggest that Jeffrey's sheltering mechanism is responsible for the weak increase in wave height whereas the wind-driven current is responsible for the downstream shift of the focusing point. For modulated wave groups, Babanin *et al.* (2010) showed that the wind forcing noticeably affects incipient breaking by stabilizing the crest shape approaching breaking onset but then randomizing the crest shape at the point of breaking. However, they argued that the wind influence on the breaking onset is marginal unless the wind forcing is very strong. The evolution of 2D dispersive focusing wave groups in deep water under wind forcing and wave breaking is investigated by Tian and Choi (2013) using a pseudo-spectral nonlinear wave model and a laboratory experiment. It was found that the model predicts the observations satisfactorily for weak wind if the wind-induced current is incorporated. The model performance, however, deteriorates for strong wind. Recent laboratory study by Saket *et al.* (2017) indicated that the presence of moderate wind forcing systematically increases the breaking onset threshold by 2%. Jou *et al.* (2021) investigated extreme wave generation through multiscale phase-amplitude coupling, phase synchronization, and self-focusing by curved crests.

Apart from direct wind forcing, the wind-induced current and current shear strength also affect the limiting steepness and crest geometries of incipient breakers. Banner and Phillips (1974) showed theoretically that the presence of a thin wind-induced drift layer can reduce the maximum surface elevation of a steady monochromatic wave at incipient breaking. Employing the dispersive focusing technique to study the freak wave formation, Wu and Yao (2004) found that while weak uniform following/opposing currents have limited influence on incipient wave breaking, strong opposing currents may cause partial wave blocking and elevate the limiting steepness up to 0.36. For vertically sheared currents, Yao and Wu (2005, 2006) observed in the laboratory that a current with a positive shear (such as the wind-driven current) reduces the steepness of an incipient unsteady breaker and increases the vertical (crest-trough) asymmetry, while a negatively sheared current (such as the jet-like ebb current at a tidal inlet) acts in the opposite way. On the other hand, Chen and Zou's (2018) model results suggested that the limiting steepness of a regular wave becomes considerably smaller (about 0.3) than that of a

Stokes wave (0.44) in the deep water in the presence of wave blocking by spatially varying opposing currents. [Chen and Zou \(2019\)](#) found that in the presence of following vertical current shear, the shallow water wave exhibits a sharper crest and flatter trough, enhancing the harmonic wave energy and the extent of triad interaction. The opposite is true in the presence of opposing vertical current shear. Following and opposing current shear may cause waves to break at a lower and higher sea state. [Guyenne \(2017\)](#) studied the effect of constant vorticity on the modulational instability of deep-water Stokes waves using a high-order spectral method. It was found that a following current with positive vorticity tends to stabilize the Stokes wave, while an opposing current with negative vorticity tends to amplify the waves thus enhancing the sideband instability.

Previous numerical studies on wave breaking under wind action have used empirical parameterizations to account for the wind pressure/drag effect (e.g., [Chen et al., 2004](#); [Kharif et al., 2008](#); [Yan and Ma, 2011](#); [Liu et al., 2015](#); [Hasan et al., 2018](#)). With recent progress of CFD (Computational Fluid Dynamics) algorithms and CPU performance, Navier–Stokes solvers coupled with an interface capturing scheme (e.g., Volume of Fluid method by [Hirt and Nichols, 1981](#); [Xie and Lin, 2022](#); [Bakhtyar et al., 2010](#); level set method by [Sethian and Smereka, 2003](#); [Wang et al., 2009](#); [Zhang et al., 2010](#); coupled VOF and level set method by [Sussman 2003](#); [Lv et al., 2010](#)) and a turbulence model have become a popular tool to examine this inherently two-phase flow problem. The air–water mixture-based formulation in two-phase models allows both wind and wave to be simulated in a single computational domain, with the air–water interface boundary conditions implicitly satisfied. Thanks to the surface capturing scheme, the complicated wave breaking process such as air entrainment can be resolved in greater detail. A few numerical studies have resorted to two-phase flow solvers to examine the wind effects on breaking waves in the surf zone ([Yan and Ma, 2009](#); [Xie, 2014, 2017](#)). For example, [Xie's \(2017\)](#) study of the wind effect on periodic waves breaking on a sloping beach showed that the presence of wind affects the wave shoaling and breaking processes and alters the airflow structure above waves. Onshore wind increases the water particle velocity and causes waves to break earlier and seaward, which is consistent with previous experiment ([Douglass, 1990](#); [King and Baker, 1996](#)). [Yan and Ma \(2010\)](#) nested a potential flow model with two-phase StarCD model to examine wind interaction with 2D freak waves.

The objective of this study is to investigate the effects of both wind direction and speed on the geometry of wave breaking, using a two-phase flow model without resorting to empirical formulations. The following/opposing wind is used instead to indicate the wind blowing in the same/opposite direction to the waves. The two-phase flow model and numerical wind-wave flume setup are described in Sec. II. After that, the wave evolution, maximum wave height, breaking location and time at breaking onset, and local wave shapes (crest steepness and asymmetry) are examined for both following and opposing winds. The separate effects of wind-driven current on wave breaking and airflow structure above the waves are also examined. Conclusions are drawn in Sec. IV.

II. METHODOLOGY

A. Two-phase flow solver

As described by [Zou and Chen \(2017\)](#), two-phase flow solvers with an interface capturing method (e.g., volume of fluid, level set) are the

state-of-the-art numerical tools to investigate the wind effects on the wave breaking problem. Without resorting to wind forcing parameterizations, the two-phase flow solver is capable of directly incorporating the overlying wind action and the accompanying drift current into the wave motion simulation. In this study, an extended two-phase flow solver built upon OpenFOAM® (Open Field Operation and Manipulation) is adopted to investigate the unsteady wave breaking under wind action. It solves the Navier–Stokes equations for two incompressible phases using a finite volume discretization and a Volume of Fluid (VOF) surface capturing method ([Jasak, 1996](#); [Rusche, 2002](#); [Weller, 2005](#)). The extended solver, *waves2Foam* ([Jacobsen et al., 2012](#)), includes new boundary conditions and utility functions for water wave and current generation and absorption using the relaxation zone technique.

The two phases of air and water are considered as one effective incompressible fluid and solved simultaneously throughout the domain. The governing equations for an incompressible two-phase flow are given by

$$\nabla \cdot \mathbf{U} = 0, \quad (1)$$

$$\begin{aligned} \frac{\partial \rho \mathbf{U}}{\partial t} + \nabla \cdot (\rho \mathbf{U} \mathbf{U}) - \nabla \cdot (\mu_{\text{eff}} \nabla \mathbf{U}) \\ = -\nabla p^* - \mathbf{g} \cdot \mathbf{X} \nabla \rho + \nabla \mathbf{U} \cdot \nabla \mu_{\text{eff}}, \end{aligned} \quad (2)$$

$$\frac{\partial \alpha}{\partial t} + \nabla \cdot (\mathbf{U} \alpha) + \nabla \cdot [\mathbf{U}_r \alpha (1 - \alpha)] = 0, \quad (3)$$

where \mathbf{U} is the fluid velocity vector, ρ is the density, p^* is the dynamic pressure, \mathbf{g} is the acceleration due to gravity, \mathbf{X} is the position vector, and $\mu_{\text{eff}} = \mu + \rho \nu_t$ is the effective dynamic viscosity, which is the sum of the molecular dynamic viscosity μ and the turbulent eddy viscosity ν_t . The turbulent eddy viscosity is calculated using the Smagorinsky subgrid-scale stress model ([Smagorinsky, 1963](#)). The volume fraction of water in a computational cell, α , serves as an indicator to mark the location of the air–water interface. Note that in Eq. (3) an extra compression term, $\nabla \cdot [\mathbf{U}_r \alpha (1 - \alpha)]$, is added to the classic VOF transport equation to limit the smearing of the interface ([Hirt and Nichols, 1981](#); [Weller, 2005](#)). \mathbf{U}_r is a velocity field introduced to compress the interface, acting only in the direction perpendicular to the interface.

The VOF function $\alpha = 1$ if the cell is full of water, $\alpha = 0$ if the cell is full of air, and $0 < \alpha < 1$ if the cell is a mixture of the two fluids. The fluid density ρ and viscosity μ in the momentum equation, Eq. (2), are given by

$$\rho = \alpha \rho_1 + (1 - \alpha) \rho_2, \quad (4)$$

$$\mu = \alpha \mu_1 + (1 - \alpha) \mu_2, \quad (5)$$

where the subscripts 1 and 2 denote water and air, respectively. An isosurface of $\alpha = 0.5$ is used to visualize the air–water interface in this study. Note that the pressure, density, and viscosity are assumed to be continuous across the air–water interface, at which no specific interface jump conditions are specified. Due to the imbalance between the dynamic pressure gradient and the density gradient, spurious air velocities may occur in the vicinity of the interface, which, in turn, may affect the wave kinematics directly beneath the instantaneous free surface ([Vukčević et al., 2017](#)). The ghost fluid method may help resolve this issue and improve the flow field prediction near the air–water interface ([Chen et al., 2022](#); [Peltonen et al., 2021](#)).

B. Numerical wind-wave flume setup

Figure 1 illustrates the present two-dimensional model setup for the wind-wave flume following Tian and Choi (2013). The physical wave tank was 15 m long and 1.5 m wide. A piston-type wavemaker was used to generate the water wave groups through dispersive focusing. At a distance of 1.49 m downstream the wavemaker, a twin-fan blower was installed on the top of the tank to generate following wind. The water depth was 0.54 m. The distance between the calm water surface and the ceiling panels (i.e., air passage gap) was 0.45 m. A breaking wave group generated at the physical wavemaker has a global steepness of $S = \sum a_n k_n = 0.57$, with constant steepness $a_n k_n$ for each of the $N = 128$ wave components of amplitude a_n and wave number k_n . The wave group has a frequency bandwidth of 1.4 Hz ranging from 1.0 to 2.4 Hz and a peak frequency of 1.1 Hz. The relative wave number is $k_p d = 2.65$ at peak frequency. It ranges from $kd = 2.22$ at $f = 1.0$ Hz to $kd = 12.51$ at $f = 2.4$ Hz, which includes both deep and intermediate water waves since the deep-water limit is $kd = 3.14$. The individual wave components of the dispersive wave group can be superimposed and brought into phase at a focus point in the flume at a specified time. This generates a realistic extreme wave event with the desired underlying spectrum. Increasing the applied maximum focused wave height leads to wave breaking at a defined location and time. Constructive interference among various components of the wave group causes a plunging breaker to occur between wave gauges G2 and G3 (Tian and Choi, 2013).

Three wind forcing conditions were considered in the experiment, the mean free stream wind speed being $U_0 = 1.4, 3.2$, and 5.0 m/s. The ratio of the free stream wind speed U_0 to the phase speed C_p of the peak wave component is $U_0/C_p = 1.0, 2.3$, and 3.6 . The wave age is $C_p/u^* = 29.2, 10.7$, and 6.4 . Thus, the strongest wind forcing considered in this study corresponds to $U_0/C_p = 3.6$ and $C_p/u^* = 6.4$. The corresponding wind speed U_{10} at the standard altitude of $z = 10$ m is $U_{10} = 1.9, 4.5$, and 7.3 m/s, which falls into the category of light to moderate breeze according to the Beaufort wind force scale. Note that U_{10} was calculated by the logarithmic law $u(z) = \frac{u^*}{\kappa} \ln(\frac{z}{z_0})$, where u^* is the wind friction velocity as measured by Tian and Choi (2013), $\kappa = 0.41$ is the von Karman constant and z_0 is the roughness length estimated from the measured wind velocity profile. Assuming the same Froude number scaling (1:60) for both the wave and wind profile, the peak wave period 0.91 s, wave height 0.084 m, and the wind speed $U_0 = 1.4, 3.2$, and 5.0 m/s simulated in this study are in full-scale conditions about 7 s, 5 m, and $U_{10} = 11, 25$, and 39 m/s. These wind speeds belong to the wind regime of breeze, gale, and hurricane

force, respectively, according to the Beaufort wind force scale. Key parameters of the wave group and the wind forcing conditions are listed in Table I.

The computational domain (Fig. 1) is 12.16 m long and 0.99 m high. Surface elevations measured at the first wave gauge G1 in the physical flume were used to drive the waves at the inlet boundary ($x = 2.84$ m) of the numerical flume. A following wind ($U_0 > 0$) is specified for the air phase at the same location as the numerical wavemaker at the left end of the flume. An opposing wind ($U_0 < 0$) is specified at the right end of the flume ($x = 15$ m), where the incoming wave is to be fully absorbed by a sponge layer. The uniform wind speed specified at wind entry is adjusted to match the free stream wind speed $|U_0| = 1.4, 3.2$, and 5.0 m/s. Two relaxation zones are used to stabilize wave generation at the inlet (left end) and wave absorption at the outlet (right end) of the flume. The bottom floor and top ceiling of the flume are treated as no-slip walls, where VOF and pressure boundary are set as zero gradient. The lateral sides (front and back) of the numerical flume are set as empty patches, which in OpenFOAM indicates that this is a 2D simulation. The time derivative in the momentum equation is discretized using the Euler scheme. The advection term and the diffusion term are discretized using a combined linear and upwind differencing scheme and a second-order linear scheme, respectively. The algebraic VOF method is used to capture the air–water interface. The pressure–velocity coupling is resolved by the PISO algorithm. The physical duration of the numerical simulation is 20 s. The time step is automatically adjusted based on the maximum Courant number limit of 0.25.

The physical experiment was conducted in a narrow long flume instead of a wide 3D tank. The wave groups generated were unidirectional. The present 2D numerical simulation is adequate to resolve the most important processes of the wave group evolution and breaking wave geometries. 3D simulation is necessary when the wind blows at an oblique angle relative to the wave. The assumption of incompressibility is appropriate for the present study but the same may not be true for other processes such as wave impact forces on structures.

A grid convergence study has been conducted to assess the grid size requirement for this problem. The computational domain is meshed non-uniformly with fine grids centered on the free surface. Three sets of grids are used; the minimum grid size near the free surface is 5.0 mm for the coarse grid, 2.5 mm for the medium grid, and 1.25 mm for the fine grid. The total number of grids is about 123 k, 464 k, and 1450 k, respectively. For the wave only case, the CPU time for the coarse, medium, and fine grid (on Intel Core i7 processor, 4 cores @3.4 GHz) is about 4, 41, and 212 h, respectively. It was found

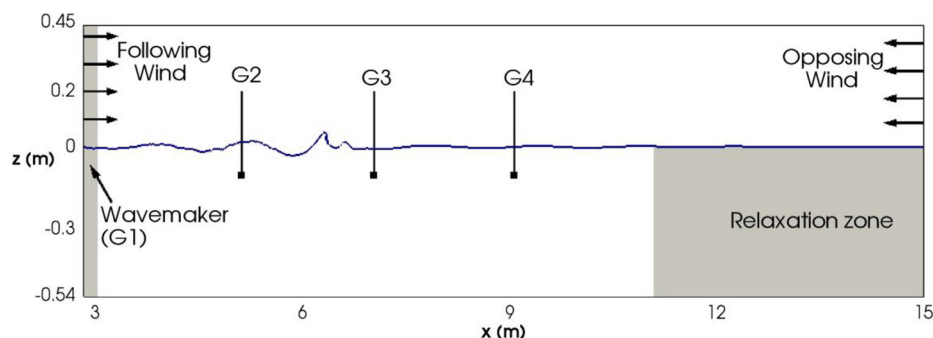


FIG. 1. Model setup for the numerical wind-wave flume (adapted from Zou and Chen, 2017). The experimental measurement at wave gauge G1 is used to drive the model. In the absence of wind, a plunging breaker occurred between wave gauges G2 and G3 (Tian and Choi, 2013).

TABLE I. Summary of wave, wind, and current parameters simulated in this study. $S = Na_p k_p$ is the global wave steepness, Δ_f is the frequency bandwidth, f_c is the center frequency, C_p is the wave celerity and the wave number k_p at peak frequency f_p , d is the water depth, U_0 is the free stream wind speed, u^* is the wind friction velocity, $U_c(z)$ is the current profile, and $U_s = 0.12$ m/s is the surface velocity and $\delta = 1$ cm the characteristic layer thickness of drift current corresponding to $U_0 = 5.0$ m/s.

Case	Wave	Wind		Current	
		Following wind	Opposing wind	Following current	Opposing current
Wave-only	$S = 0.57$ $\Delta_f = 1.4$ Hz $f_c = 1.7$ Hz $f_p = 1.1$ Hz $k_p d = 2.65$				
Wave + Wind (current)	Same as above	$U_0 = 1.4, 3.2, 5.0$ m/s $U_0/C_p = 1.0, 2.3, 3.6$ $C_p/u^* = 29.2, 10.7, 6.4$	$U_0 = -1.4, -3.2, -5.0$ m/s $U_0/C_p = -1.0, -2.3, -3.6$ $C_p/u^* = -29.2, -10.7, -6.4$	Wind-driven	Wind-driven
Wave + Current	Same as above	-	-	$U_c(z) = U_s \exp(z/\delta)$	$U_c(z) = -U_s \exp(z/\delta)$

that the simulation results using both the medium and the fine grid are in good agreement with the experimental data, especially for wave gauges (G3 and G4) downstream the breaking region. The medium grid was, thus, used in all the ensuing simulations. In the presence of following wind, the computational time is about 100 h for $U_0 = 3.2$ m/s and 320 h for $U_0 = 5.0$ m/s.

C. Wind-driven current

As wind blows over the water surface, a thin surface drift appears in the water due to the overlying wind shear (Wu, 1975; Longo *et al.*, 2012). Zou and Chen (2017) showed that the current velocity decreases sharply from its surface value to nearly zero within a thin layer and that the current profile may be approximated by the exponentially decaying function $U_c(z) = U_s \exp(z/\delta)$, where U_s is the current velocity at the surface, z is the vertical coordinate positive upward from the still water level, and δ is a characteristic layer thickness of the drift current. Wu (1975) observed that the surface drift current velocity can be related to the wind friction velocity u^* by $U_s = 0.55 u^*$. In the presence of a following wind speed $U_0 = 5.0$ m/s, the present two-phase model predicted $U_s \simeq 0.12$ m/s and $\delta \simeq 1$ cm (see Fig. 9 in Zou and Chen, 2017). The predicted current is consistent with the measured wind friction velocity by Tian and Choi (2013) and resembles the observed wind drift current profiles by Longo *et al.* (2012).

It is assumed that wind action affects the wave group evolution through the combined effects of direct wind forcing which leads to a pressure differential around the wave crest and thereby directly altering the crest kinematics and wind-driven current, which causes Doppler shifts to the waves [see Fig. 2(a) for illustration]. In comparison with the combined effects of direct wind forcing and drift current on the wave breaking process, the separate effect of the wind drift current is, thus, investigated by initializing the wind-wave flume with a steady wind-driven current field and superimposing the current profile with the wave velocities at the wave-maker. Table I lists the detailed wave, wind, and current parameters to be simulated in this study. Readers may refer to Zou and Chen (2017) for the specification of initial and boundary conditions to examine the wind-wave and wave-current interactions.

III. RESULTS AND DISCUSSIONS

A. Wave evolution in the presence of wind

The present numerical model has been validated by Zou and Chen (2017) for a non-breaking wave group against physical experiment with and without the following wind. Figure 3 shows the comparison of the surface elevation history at 4 wave gauges of a plunging breaking wave group between the present VOF-based two-phase flow model, experiment, and the pseudo-spectral model by Tian and Choi (2013). It should be noted that the pseudo-spectral model is a single-phase model considering only the water phase with the surface wind pressure specified by a combined Miles and Jeffrey's model. In contrast, the present model considers both airflow and water motion in a single computational domain without empirical assumptions. By comparison, the present model results have better phase agreements (at G3-G4) with the experimental data, largely due to the more realistic drift current profile predicted by the present model. According to linear wave theory, surface elevation squared is a measure of the total wave energy. The predicted surface elevation history is validated with measurements at separate wave gauges; therefore, the predicted and observed total mechanical energy is also consistent with each other at these locations (Tian and Choi, 2013).

Figures 4 and 5 show the snapshot comparison of wave profiles and vorticity contours under different following and opposing wind speeds, respectively. It is seen that in the presence of following winds (Fig. 4), the wave without wind action experiences the earliest breaking in time, followed by the wave forced by increasingly stronger following winds from $U_0 = 1.4$ to 5.0 m/s. Corresponding to the delay of the breaking time is the downwave shift of the breaking location with increasing wind speeds. At the same instant $t = 22.85$ s [Fig. 4(b)], the wave under a strong following wind $U_0 = 3.2$ and 5.0 m/s has just started the breaking process, i.e., the initiation of overturning jet, while the wave under a weak wind $U_0 = 1.4$ m/s has reached the stage of oblique splash-up. An air bubble is formed as the overturning jet plunges into the wave trough ahead. In comparison, the wave without wind action has experienced decreased wave crest elevation and a strong vertical jet following the prior oblique splash-up process.

In the presence of opposing winds (Fig. 5), the trend of breaking time and location is in the opposite sequence to that under following

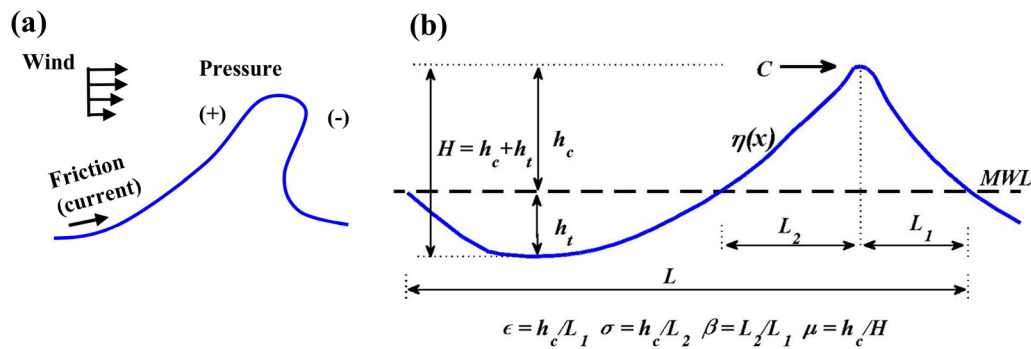


FIG. 2. (a) Illustration of the wind actions on the waves including wind friction induced surface layer current and form drag due to the pressure differential across the wave crest and (b) definition of local wave shape parameters following Kjeldsen and Myrhaug (1979). ϵ and σ are the crest-front and crest-rear steepness, respectively. β and μ are the horizontal and vertical asymmetry, respectively. The vertical (crest-trough) asymmetry is also known as skewness. MWL stands for mean water level.

winds. While an overturning jet just appears for the wave without wind action, the wave under the opposing wind $U_0 = -1.4$ and -3.2 m/s has completed the jet-plunging process. The jet strength under the opposing wind $U_0 = -3.2$ m/s is apparently weaker than that under $U_0 = -1.4$ m/s. In contrast, the wave under the stronger opposing wind $U_0 = -5.0$ m/s exhibits no major breaking events. The strong wind forcing and the accompanying opposing drift current are of sufficient strength to alter the wave group focusing process, which makes the originally expected large wave crest disappear. The wave crest for this case is now leaning backward, instead of forward as in the other cases with wave breaking.

It is evident from Fig. 6(d) that the wave group plunges in the absence of wind. In the presence of the strongest wind forcing studied ($U_0 = -5.0$ m/s), the breaking is suppressed. Thus, it is reasonable to speculate that at intermediate wind speeds such as $U_0 = -3.2$ m/s, the wave group may have experienced a spilling-type wave breaking. Correspondingly, with increasing opposing wind speed, the air bubble entrapped as the plunging jet impinges on the free surface may first shrink in size and then disappear entirely. As shown in Fig. 4, the following wind may initiate wave breaking and elongate the first plunging jet and, therefore, increase the entrained air volume and breaking intensity by increasing the water particle velocity at the crest. To fully

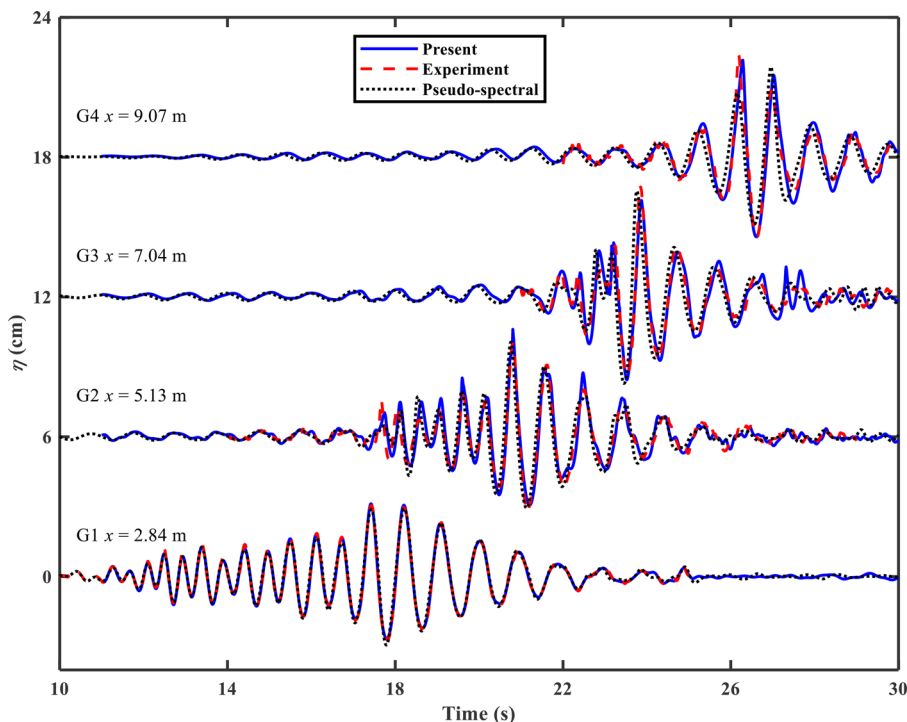


FIG. 3. Surface elevation time history at 4 wave gauges (G1–G4) under a following wind $U_0 = 3.2$ m/s. Solid line: the present two-phase model; dashed and dotted lines: experiment and single-phase pseudo-spectral model by Tian and Choi (2013). The surface elevations at G2–G4 have been shifted by a multiple of 6 cm to show the wave group evolution.

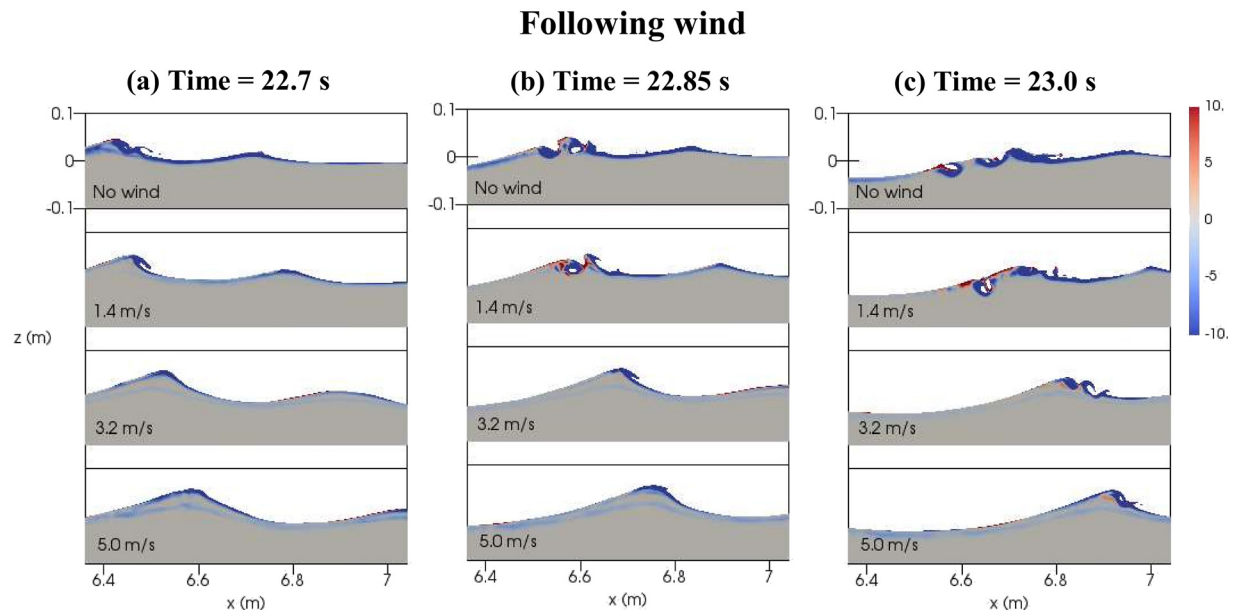


FIG. 4. Snapshots of wave profiles and vorticity in water (color contour, unit in s^{-1}) under a following wind speed of $U_0 = 1.4, 3.2$, and 5.0 m/s (from top to bottom) at time (a) 22.7 s, (b) 22.85 s, and (c) 23.0 s. Waves propagate from left to right while the following wind acts on the wave in the same direction. Relative free stream wind speed $U_0/C_p = 1.0, 2.3$, and 3.6 , where C_p is the phase speed of the peak wave component. The corresponding wave age is $C_p/u^* = 29.2, 10.7$, and 6.4 , where u^* is the wind friction velocity.

resolve and quantify the volume/area of the entrapped air by the plunging breaker, however, very fine grid and possible 3 D simulation are necessary.

B. Airflow and wave profile under wind and current action

The airflow structure above the waves, which causes form drag due to the presence of evolving wave crests, is examined by separating the wind-induced drift current effect from the combined form drag and drift current effects. Figure 6 compares the effects of following/opposing drift current and wind on the wave profiles and airflow field near the breaking location. The airflow field above the wave crest with the following/opposing drift current effect is similar in pattern to those without wind (Zou and Chen, 2017), both driven by the wave crest motion underneath. As the wave crest propagates to the right, the air escaping the approaching crest flows upward and recirculates around the crest to the rear face of the crest. However, the airflow field under wind action is mainly dominated by the wind speed relative to the wave and the wave shape. In the presence of the following wind, the air flow accelerates as it climbs up and passes over the breaking crest. Beyond the overturning crest front is the airflow separation, which sheds vortices rising high above the water surface and likely enhances the turbulent mixing in the air. The predicted airflow structure is similar to that over a backward-facing step (Reul et al., 2008; Buckley and Veron, 2016; Sullivan et al., 2018). In the presence of opposing wind [Fig. 5(d)], the airflow separation occurs at the rear face of the crest, confirming that wave breaking is not a prerequisite for airflow separation. Due to the larger (opposing) wind speed relative to the wave crest speed, the vortex strength seems to be much stronger than that under following wind. The airflow structure is similar to that over an airfoil

at high angles of attack. Both primary vortices and secondary vortices with opposite signs appear, which interact with each other with a bounding but moving free surface underneath. These vortices are advected downwind and gradually lose their strength. Accompanying the airflow separation is a pressure drop in the lee of the wave crest, which leads to a positive/negative form drag in the presence of following/opposing wind (Zou and Chen, 2017).

By imposing a positive form drag on the wave crest, the following wind forcing may accelerate the breaking by directly altering the crest kinematics. It is apparent that the wave breaking under the following wind [Fig. 6(b), both form drag and drift current] occurs earlier compared to the case with only wind-induced drift current [Fig. 6(a)]. However, both cases have a breaking location far away from the case without any wind/current effect [see also Fig. 6(b)]. On the other hand, by imposing a negative form drag on the wave crest, the opposing wind forcing may weaken the crest motion and make the plunging breaking disappear. It is seen that while the wave under opposing drift current [Fig. 6(c)] shows an overturning crest front, the wave under opposing wind [Fig. 6(d)], both form drag and drift current] exhibits no sign of plunging breaking (see also Fig. 5). The large wave crest for both cases is located around $x = 6.05$ m, upwave from the breaking location $x_b = 6.26$ m without wind or current effect. This suggests that while the form drag arising from the direct wind forcing may be responsible for the wave breaking type, therefore, intensity and wave shape at the crest, the wind-driven current has a dominant effect on the shift of the breaking location. The wave profile under the strong following wind in Fig. 6(b) resembles that under the opposing wind-induced drift current in Fig. 6(c) and the wave profile under the strong opposing wind in Fig. 6(d) resembles that under the following wind-induced drift current in Fig. 6(a).

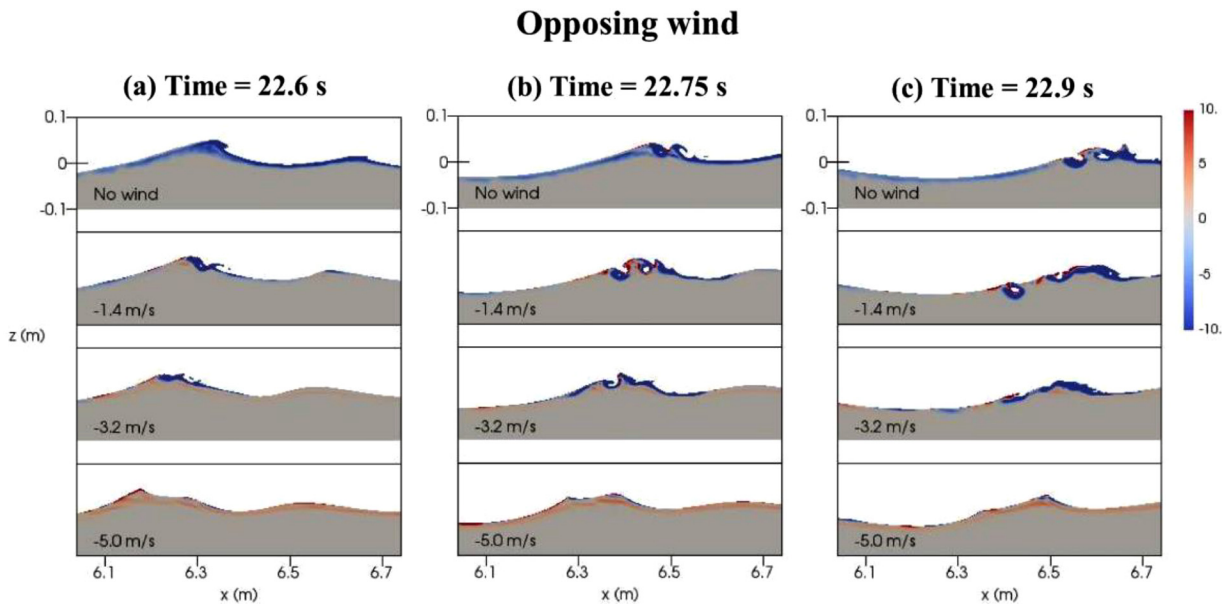


FIG. 5. Same as Fig. 4 but for opposing wind speeds of $U_0 = -1.4, -3.2$, and -5.0 m/s at time (a) 22.6 s, (b) 22.75 s, and (c) 22.9 s. Waves propagate from left to right while the opposing winds act on the waves in the opposite (from right to left) direction. Relative free stream wind speed is $U_0/C_p = -1.0, -2.3$, and -3.6 . The corresponding wave age is $C_p/U^* = -29.2, -10.7$, and -6.4 .

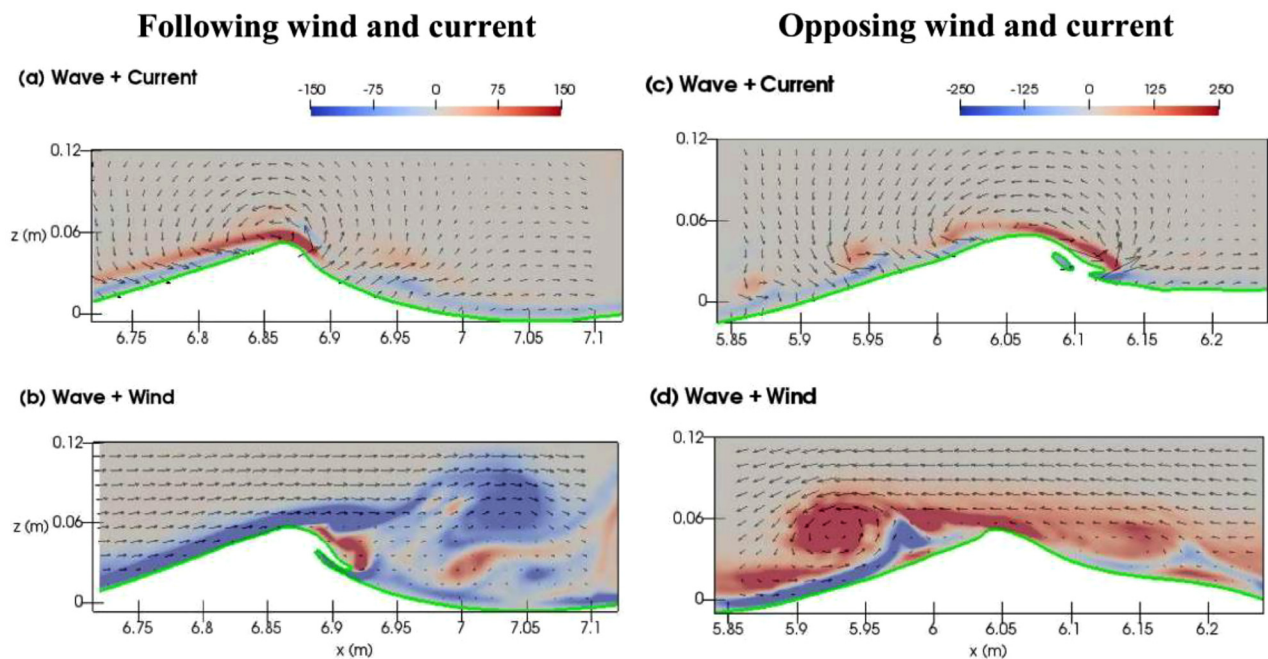


FIG. 6. Instantaneous snapshots of wave profiles (thick green lines), airflow field (arrows), and vorticity (color contours, unit in s^{-1}) in the presence of following (a) current and (b) wind at $t = 22.95$ s and opposing (c) current and (d) wind at $t = 22.45$ s. [(a), (c)] Wind-induced following/opposing drift current is superimposed with the waves at the wave-maker. [(b), (d)] Wind speed $U_0 = \pm 5.0$ m/s is imposed at the wind inlet so that the waves are affected by wind drift current as well as direct wind forcing. Note that the scales of vector arrows in (a) and (c) are one-tenth of those in (b) and (d), where the free stream wind speed is $|U_0| = 5.0$ m/s. Relative free stream wind speed $|U_0/C_p| = 3.6$ and wave age $C_p/U^* = 6.4$.

C. Wave height and location and time of breaking

Figure 7 shows the following/opposing wind effects on the maximum wave height H and the location x_b and time t_b of breaking, i.e., when the crest front becomes vertical. The maximum wave height increases slightly with stronger following wind and decreases overall for the opposing wind, except for the noticeable increase at $U_0 = -3.2$ m/s. The overall decrease in the wave height under opposing wind is primarily due to the direct wind forcing (negative form drag) that inhibits the wave growth and secondarily to the non-optimal focusing as a result of drift current effect. The noticeable increase at $U_0 = -3.2$ m/s arises from probably the dominant effect of the opposing current, which tends to shorten the wavelength and increase the wave height, over the direct wind forcing. The opposing drift current modifies the wave number and, hence, may cause the wave group to focus at a new location. The steady increase in the wave height with

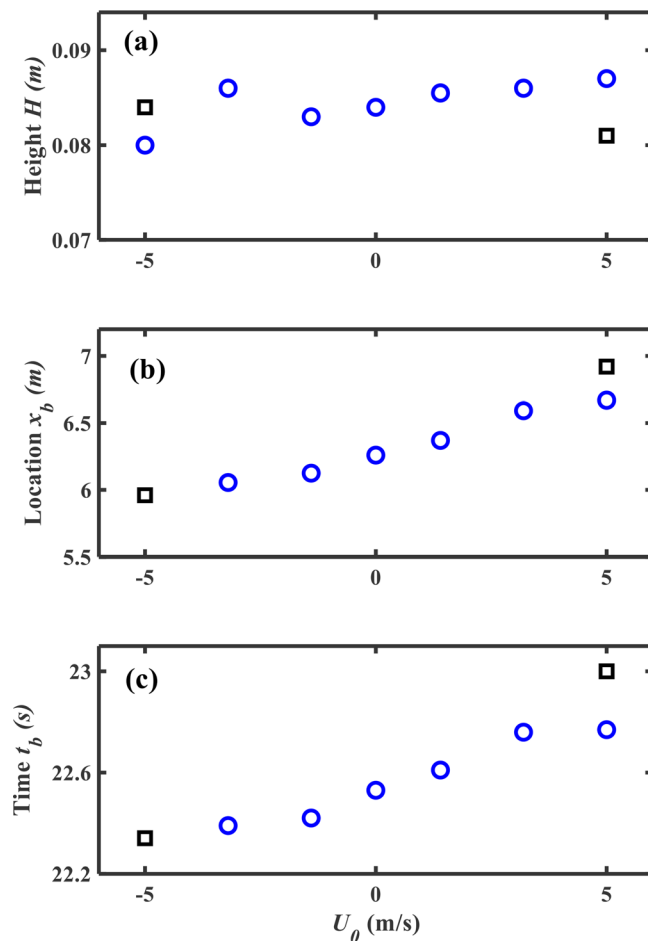


FIG. 7. The effects of following wind speed ($U_0 > 0$) and opposing wind speed ($U_0 < 0$) on (a) maximum wave height, (b) breaking location, and (c) breaking time. Circles: wave + wind (combined form drag and drift current). Squares: wave + wind-induced drift current for $|U_0| = 5.0$ m/s. Free stream wind speeds $|U_0| = 1.4, 3.2, 5.0$ m/s correspond to $|U_0|/C_p = 1.0, 2.3, 3.6$ and $C_p/|u^*| = 29.2, 10.7, 6.4$, where C_p is the phase speed of the peak wave component and u^* is the wind friction velocity.

following wind speed is due to increased direct wind forcing (positive form drag) that imparts momentum and energy to the wave and enhanced wave focusing by the wind-induced drift current. For a wave group with large initial steepness, the largest wave crest will grow unstable and thus break prematurely before reaching the maximum wave height at the theoretical focusing point. In the presence of following wind, the wind-induced drift current shifts the theoretical focusing point further downstream (Kharif *et al.*, 2008; Zou and Chen, 2017), thereby allowing the wave group to continue the focusing process.

Consistent with the analysis above on the wind-driven current effect and non-optimal/continual focusing, the wave breaking location and time are shifted (see also Figs. 4 and 5). The following wind shifts the breaking location downstream and delays the breaking, vice versa for the opposing wind. The stronger the wind action, the larger shifts of the breaking location/time, which are approximately linearly proportional to the wind speed under weak winds and saturate under strong winds. Similar to the shifts of focusing point in a non-breaking wave group (Zou and Chen, 2017), the shifts of the breaking location/time in the present plunging breaking wave group are mainly attributed to the wind-driven current (see squares in Fig. 7). It is worth noting that the wave under following wind $U_0 = 5.0$ m/s breaks almost at the same time as that under $U_0 = 3.2$ m/s, indicating the increasing importance of wind forcing effect on wave breaking under strong wind. For example, when only the following drift current corresponding to a wind speed of $U_0 = 5.0$ m/s is present, the wave breaks at $t_b = 23.0$ s and $x_b = 6.92$ m. The presence of additional direct wind forcing, however, makes the wave break earlier at $t_b = 22.77$ s at an upstream location $x_b = 6.67$ m. On the other hand, when only the opposing drift current corresponding to a wind speed of $U_0 = -5.0$ m/s is present, wave breaking is still observed; when the additional direct wind forcing is imposed, however, wave breaking is no longer observable (see also Fig. 5). The strong opposing wind forcing reduces the maximum wave height and prevent the major wave breaking from happening, while the strong following wind forcing increases the maximum wave height and causes early initiation of wave breaking.

D. Local wave shape at the breaking onset

Figures 8(a) and 8(b) show the wind effects on the local crest front and rear steepness at the wave breaking onset [see Fig. 2(b) for definitions], when the crest front becomes vertical and, thus, breaking is bound to occur thereafter. The front steepness [Fig. 8(a)] for all wind speeds has a value larger than 0.4, a typical lower bound for a plunging breaker to occur (Perlin *et al.*, 2013). Because of wave crest's leaning forward at breaking onset, the rear steepness [Fig. 8(b)] is overall smaller than the front steepness. It is worth noticing that the front steepness reduces to 0.42 for opposing wind speed $U_0 = -3.2$ m/s. Increasing the strength of the opposing wind speed $U_0 = -5.0$ m/s would reduce the crest front steepness further and prevent the breaker from happening (therefore, no circles present at this point). The front steepness under opposing drift current ($U_0 = -5.0$ m/s) is below 0.4, whereas a plunging breaker is still observed [see Fig. 6(c)]. This is related to the definition of the zero-down crossing point preceding the breaking crest [Fig. 2(b)]. For breaking waves in a dispersive focusing group in general (Tian *et al.*, 2012) and this case in particular, the trough in front of the breaking crest rises above the mean water level, causing the immediate zero-down crossing point between crest and

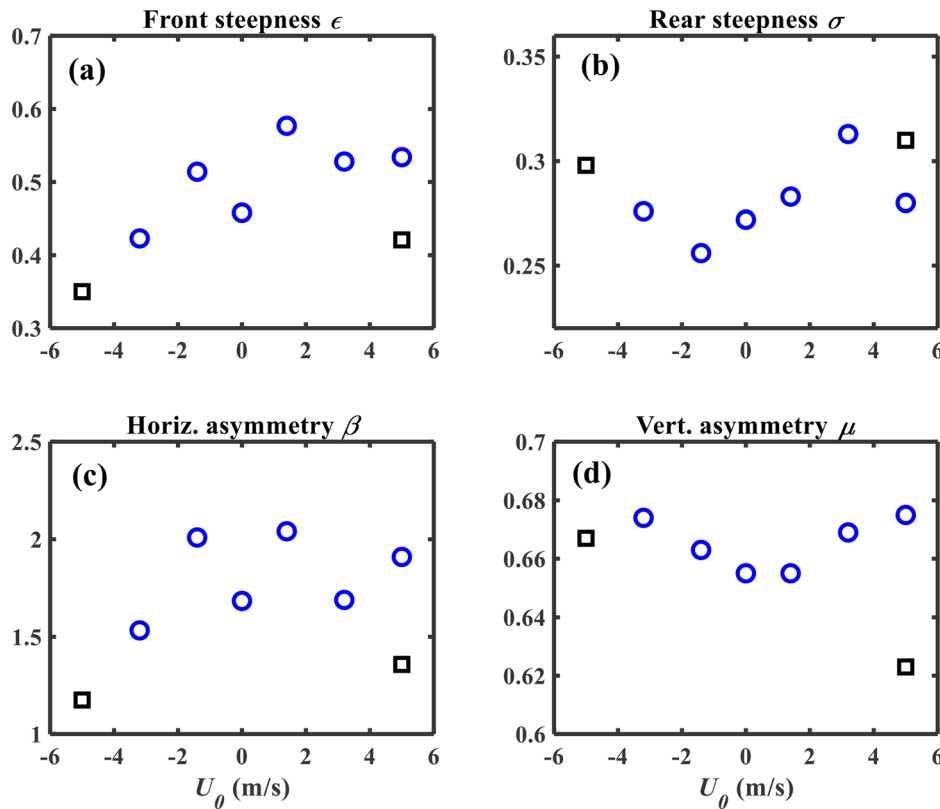


FIG. 8. The effects of following wind speed ($U_0 > 0$) and opposing wind speed ($U_0 < 0$) on (a) front steepness, (b) rear steepness, (c) horizontal asymmetry (wave asymmetry), and (d) vertical asymmetry (wave skewness) of local wave crests at breaking onset, i.e., the crest front becomes vertical. Blue circles: wave + wind (combined form drag and drift current). Black squares: wave + drift current for $|U_0| = 5.0$ m/s. See Fig. 2(b) for the definitions of the wave shape geometric properties. Free stream wind speeds $|U_0| = 1.4, 3.2, 5.0$ m/s correspond to $|U_0|/C_p = 1.0, 2.3, 3.6$ and $C_p/|u^*| = 29.2, 10.7, 6.4$, where C_p is the phase speed of the peak wave component and u^* is the wind friction velocity.

trough to disappear. This leads to a smaller front steepness than that expected for a typical plunging breaker.

Figures 8(c) and 8(d) show the horizontal and vertical asymmetry at breaking onset. For all the cases considered, the horizontal asymmetry has a value above 1.0, which indicates that all the breaking crests lean forward in the propagating direction of the wave group. The smallest value of horizontal asymmetry is 1.1, which occurs for the wave under opposing drift current ($U_0 = -5.0$ m/s). The additional wind forcing reduces the horizontal asymmetry further below 1.0 and causes the crest to start to lean backward [see Figs. 5 and 6(d)]. The vertical asymmetry does not vary much with the wind speeds. One noticeable exception is the case under the following wind-induced drift current ($U_0 = 5.0$ m/s), which reduces the vertical asymmetry from 0.67 with additional wind forcing to 0.62 without. This reduction is mainly due to the decreased crest elevation by the wind-induced drift current only [see Fig. 7(a)], which is consistent with the theoretical analysis for a steady wave train by Banner and Phillips (1974).

Zdyrski and Feddersen (2020, 2021) proved theoretically through a multiple-scale perturbation analysis that the wind effects on wave shapes are qualitatively similar in intermediate to deep water and in shallow water and that the effects are more pronounced for waves in shallow water. They found that for progressive regular waves, the following/onshore and opposing/offshore wind increases and decreases the wave height and skewness (crest-trough asymmetry), respectively. For the dispersive focusing wave group considered in this study, the presence of wind-driven current, which shifts the wave group's

focusing and thus breaking process, makes examining the wind effects on wave shapes more complicated. The wave group was mechanically generated by the wavemaker at the inlet and then forced by following and opposing winds. The youngest wave age considered is $C_p/u^* = 6.4$, which may not be as young as those by Zdyrski and Feddersen (2020, 2021), and thus, the direct wind effects may be not as pronounced as those over wind-generated waves. Our studies indicate that the following wind increases slightly the maximum wave height and skewness, and the wind drift current serves mainly to shift the wave group's focusing/breaking location in the downwave direction. However, the opposing wind may also increase the maximum wave height at one point because of the opposing wind drift current induced (upwave) refocusing of the wave group. Eventually, strong opposing wind decreases the wave height and skewness.

IV. CONCLUSIONS

Wind effects on the wave breaking process of a dispersive focusing wave group are investigated using a two-phase flow model, with special attention to the opposing wind and breaking wave geometry. The model solves the Navier–Stokes equations for both air and water and captures the air–water interface using the volume of fluid method and turbulence by the Smagorinsky subgrid-scale model. The model predictions compare well with the experimental data without wind and with the following wind. The effect of the wind direction on the wave breaking process is then examined by comparisons of following and opposing wind

model results. The effects of wind forcing on the local wave geometries at breaking increase with wind speed. The wave shape before, during, and after breaking is significantly altered by strong wind. The wave shape changes are qualitatively similar to the theoretical results by Zdyrski and Feddersen (2020, 2021) for regular waves, i.e., the following and opposing wind increases and decreases the wave height and skewness (crest-trough wave asymmetry), respectively. Under the same wind speed, the opposing wind has more pronounced effect on the wave shape than the following wind. We observed that a strong opposing wind forcing up to $U_0/C_p = 3.6$ and $C_p/u^* = 6.4$ may even cause the wave crest tilt backwards and prevent the plunging breaker from occurring at all. The aforementioned wind influence on wave shape and breaking type, in turn, would alter the breaking-induced wave energy dissipation since it is proportional to the breaking strength parameter, which is a function of the breaking wave geometry (Phillips, 1985; Romero *et al.*, 2012; Pizzo and Melville, 2013). The airflow structure above the wave crest is also affected by the wind speed and direction, which, in turn, influences the energy and momentum transfer from wind to wave (Agnon *et al.*, 2005).

In the absence of wind, a single plunging breaker was observed for the dispersive focusing wave group. The major wave breaking events, namely, overturning jet, plunging, air entrainment, splash-up, and vertical jet, are well captured by the two-phase flow model. In comparison with the wave breaking process without wind, the following wind delays the breaking process and shifts the breaking location downstream. The opposite is true for the opposing wind. The shift of breaking location/time is approximately linearly proportional to the wind speed (drift current) under weak winds, but the shift saturates under strong winds. Numerical results suggest that the wind-induced drift current is mainly responsible for the shifts of the breaking time/location. With increasing wind speeds, the direct wind forcing plays an increasingly more important role in affecting the maximum wave height and the breaking process. The airflow separating from the wave crest creates a sheltered region in the lee of the crest, thereby affecting the crest dynamics through form drag. The strong following wind forcing may initiate earlier wave breaking by increasing the water particle velocity at the crest, while the opposing wind forcing may initiate weaker wave breaking by decreasing the water particle velocity at the crest and may be strong enough to inhibit crest height growth and make the plunging breaker disappear.

ACKNOWLEDGMENTS

The authors acknowledge the support of the Physical Oceanography Program of National Science Foundation (NSF) of U.S. under Award No. 1436642 and the computational support provided by the Advanced Computing Group at the University of Maine system. The authors also would like to thank Dr. Zhilong Liu for discussions. Haifei was indebted to the Correll and the George & Caterina Sakellaris Graduate Fellowship for supporting part of his Ph.D. study.

AUTHOR DECLARATIONS

Conflict of Interest

The authors have no conflicts to disclose.

Author Contributions

Haifei Chen: Conceptualization (equal); Investigation (equal); Methodology (equal); Validation (equal); Writing – original draft (equal); Writing – review & editing (equal). **Qingping Zou:** Conceptualization (equal); Methodology (equal); Project administration (equal); Resources (equal); Supervision (equal); Writing – review & editing (equal).

DATA AVAILABILITY

The data that support the findings of this study are available from the corresponding author upon reasonable request.

REFERENCES

- Agnon, Y., Babanin, A. V., Young, I. R., and Chalikov, D., "Fine scale inhomogeneity of wind-wave energy input, skewness, and asymmetry," *Geophys. Res. Lett.* **32**(12), L12603 (2005).
- Babanin, A. V., Chalikov, D., Young, I. R., and Savelyev, I., "Numerical and laboratory investigation of breaking of steep two-dimensional waves in deep water," *J. Fluid Mech.* **644**, 433–463 (2010).
- Bakhtyar, R., Razmi, A. M., Barry, D. A., Yeganeh-Bakhtyari, A., and Zou, Q., "Air-water two-phase flow modeling of turbulent surf and swash zone wave motions," *Advances in Water Resources* **33**(12), 1560–1574 (2010).
- Banner, M. L., and Peregrine, D. H., "Wave breaking in deep water," *Annu. Rev. Fluid Mech.* **25**(1), 373–397 (1993).
- Banner, M. L., and Phillips, O. M., "On the incipient breaking of small scale waves," *J. Fluid Mech.* **65**, 647–656 (1974).
- Barthelemy, X., Banner, M. L., Peirson, W. L., Fedele, F., Allis, M., and Dias, F., "On a unified breaking onset threshold for gravity waves in deep and intermediate depth water," *J. Fluid Mech.* **841**, 463–488 (2018).
- Buckley, M. P., and Veron, F., "Structure of the airflow above surface waves," *J. Phys. Oceanogr.* **46**(5), 1377–1397 (2016).
- Bullock, G. N., Obhrai, C., Peregrine, D. H., and Bredmose, H., "Violent breaking wave impacts. Part 1: Results from large-scale regular wave tests on vertical and sloping walls," *Coastal Eng.* **54**(8), 602–617 (2007).
- Chella, M. A., Bihs, H., Myrhaug, D., and Muskulus, M., "Hydrodynamic characteristics and geometric properties of plunging and spilling breakers over impermeable slopes," *Ocean Modell.* **103**, 53–72 (2016).
- Chen, H., and Zou, Q., "Characteristics of current-induced wave breaking and blocking by spatially varying opposing currents," *J. Geophys. Res. Oceans* **123**(5), 3761–3785, <https://doi.org/10.1029/2017JC013440> (2018).
- Chen, H., and Zou, Q., "Effects of following and opposing vertical current shear on nonlinear wave interactions," *Appl. Ocean Res.* **89**, 23–35 (2019).
- Chen, Q., Kaihatu, J. M., and Hwang, P. A., "Incorporation of wind effects into Boussinesq wave models," *J. Waterway, Port, Coastal, Ocean Eng.* **130**(6), 312–321 (2004).
- Chen, S., Zhao, W., and Wan, D., "On the scattering of focused wave by a finite surface-piercing circular cylinder: A numerical investigation," *Phys. Fluids* **34**(3), 035132 (2022).
- Crawford, A. M., and Hay, A. E., "Linear transition ripple migration and wave orbital velocity skewness: Observation," *J. Geophys. Res.* **106**(C7), 14113–14128, <https://doi.org/10.1029/2000JC000612> (2001).
- Dias, F., and Ghidaglia, J. M., "Slamming: Recent progress in the evaluation of impact pressures," *Annu. Rev. Fluid Mech.* **50**, 243–273 (2018).
- Doering, J. C., and Bowen, A. J., "Skewness in the nearshore zone: A comparison of estimates from Marsh-McBirney current meters and colocated pressure sensors," *J. Geophys. Res.* **92**(C12), 13173–13183, <https://doi.org/10.1029/JC092iC12p13173> (1987).
- Douglass, S. L., "Influence of wind on breaking waves," *J. Waterway, Port, Coastal, Ocean Eng.* **116**(6), 651–663 (1990).
- Drazen, D. A., Melville, W. K., and Lenain, L. U. C., "Inertial scaling of dissipation in unsteady breaking waves," *J. Fluid Mech.* **611**, 307–332 (2008).
- Duncan, J. H., "Spilling breakers," *Annu. Rev. Fluid Mech.* **33**, 519–547 (2001).
- Feddersen, F., and Veron, F., "Wind effects on shoaling wave shape," *J. Phys. Oceanogr.* **35**(7), 1223–1228 (2005).

- Galchenko, A., Babanin, A. V., Chalikov, D., Young, I. R., and Haus, B. K., "Influence of wind forcing on modulation and breaking of one-dimensional deep-water wave groups," *J. Phys. Oceanogr.* **42**(6), 928–939 (2012).
- Guyenne, P., "A high-order spectral method for nonlinear water waves in the presence of a linear shear current," *Comput. Fluids* **154**, 224–235 (2017).
- Hasan, S. A., Sriram, V., and Selvam, R. P., "Numerical modelling of wind-modified focused waves in a numerical wave tank," *Ocean Eng.* **160**, 276–300 (2018).
- Hirt, C. W., and Nichols, B. D., "Volume of fluid (VOF) method for the dynamics of free boundaries," *J. Comput. Phys.* **39**(1), 201–225 (1981).
- Hoefel, F., and Elgar, S., "Wave-induced sediment transport and sandbar migration," *Science* **299**(5614), 1885–1887 (2003).
- Hsu, T. J., Elgar, S., and Guza, R. T., "Wave-induced sediment transport and onshore sandbar migration," *Coastal Eng.* **53**(10), 817–824 (2006).
- Jacobsen, N. G., Fuhrman, D. R., and Fredsoe, J., "A wave generation toolbox for the open-source CFD library: OpenFoam[®]," *Int. J. Numer. Meth. Fluids* **70**(9), 1073–1088 (2012).
- Jasak, H., "Error analysis and estimation for the finite volume method with applications to fluid flows," Ph.D. thesis (Imperial College London, 1996).
- Jiang, C., Yang, Y., and Deng, B., "Study on the nearshore evolution of regular waves under steady wind," *Water* **12**(3), 686 (2020).
- Jou, J. L., Lo, W. S., and I, L., "Rogue wave generation in wind-driven water wave turbulence through multiscale phase-amplitude coupling, phase synchronization, and self-focusing by curved crests," *Phys. Fluids* **33**(10), 102105 (2021).
- Kharif, C., Giovanangeli, J. P., Touboul, J., Grare, L., and Pelinovsky, E., "Influence of wind on extreme wave events: Experimental and numerical approaches," *J. Fluid Mech.* **594**, 209–247 (2008).
- Kiger, K. T., and Duncan, J. H., "Air-entrainment mechanisms in plunging jets and breaking waves," *Annu. Rev. Fluid Mech.* **44**, 563–596 (2012).
- King, D. M., and Baker, C. J., "Changes to wave parameters in the surf zone due to wind effects," *J. Hydraul. Res.* **34**, 55–76 (1996).
- Kjeldsen, S. S., and Myrhaug, D. S., "Breaking waves in deep water and resulting wave forces," in *Proceedings of Annual Offshore Technology Conference*, New York, 1979.
- Liu, K., Chen, Q., and Kaihatu, J. M., "Modeling wind effects on shallow water waves," *J. Waterw. Port Coast Ocean Eng.* **142**(1), 04015012 (2015).
- Longo, S., Liang, D., Chiapponi, L., and Jiménez, L. A., "Turbulent flow structure in experimental laboratory wind generated gravity waves," *Coastal Eng.* **64**, 1–15 (2012).
- Lv, X., Q. Zou, Y. Zhao, and D. Reeve, "A novel coupled level set and volume of fluid method for sharp interface capturing on 3D tetrahedral grids," *J. Comput. Phys.* **229**, 2573–2604 (2010).
- Melville, W. K., "The role of surface-wave breaking in air-sea interaction," *Annu. Rev. Fluid Mech.* **28**, 279–321 (1996).
- O'Dea, A., Brodie, K., and Elgar, S., "Field observations of the evolution of plunging-wave shapes," *Geophys. Res. Lett.* **48**(16), e2021GL093664, <https://doi.org/10.1029/2021GL093664> (2021).
- Oh, S. H., Mizutani, N., Suh, K. D., and Hashimoto, N., "Experimental investigation of breaking criteria of deepwater wind waves under strong wind action," *Appl. Ocean Res.* **27**, 235–250 (2005).
- Peltonen, P., Kanninen, P., Laurila, E., and Vuorinen, V., "Scaling effects on the free surface backward facing step flow," *Phys. Fluids* **33**(4), 042106 (2021).
- Peng, Z., Zou, Q., Reeve, D., and Wang, B., "Parameterisation and transformation of wave asymmetries over a low-crested breakwater," *Coastal Eng.* **56**(11), 1123–1132 (2009).
- Peregrine, D. H., "Water-wave impact on walls," *Annu. Rev. Fluid Mech.* **35**(1), 23–43 (2003).
- Perlin, M., Choi, W., and Tian, Z., "Breaking waves in deep and intermediate waters," *Annu. Rev. Fluid Mech.* **45**, 115–145 (2013).
- Phillips, O. M., "Spectral and statistical properties of the equilibrium range in wind-generated gravity waves," *J. Fluid Mech.* **156**, 505–531 (1985).
- Pizzo, N. E., and Melville, W. K., "Vortex generation by deep-water breaking waves," *J. Fluid Mech.* **734**, 198–218 (2013).
- Reul, N., Branger, H., and Giovanangeli, J. P., "Air flow separation over unsteady breaking waves," *Phys. Fluids* **11**, 1959–1961 (1999).
- Reul, N., Branger, H., and Giovanangeli, J. P., "Air flow structure over short-gravity breaking water waves," *Boundary-Layer Meteorol.* **126**(3), 477–505 (2008).
- Roelvink, J. A., and Stive, M. J. F., "Bar-generating cross-shore flow mechanisms on a beach," *J. Geophys. Res.* **94**(C4), 4785–4800, <https://doi.org/10.1029/JC094iC04p04785> (1989).
- Romero, L., Melville, W. K., and Kleiss, J. M., "Spectral energy dissipation due to surface wave breaking," *J. Phys. Oceanogr.* **42**(9), 1421–1444 (2012).
- Ruessink, B. G., Ramaekers, G., and Van Rijn, L. C., "On the parameterization of the free-stream non-linear wave orbital motion in nearshore morphodynamic models," *Coastal Eng.* **65**, 56–63 (2012).
- Rusche, H., "Computational fluid dynamics of dispersed two-phase flows at high phase fractions," PhD thesis (Imperial College London, 2002).
- Saket, A., Peirson, W. L., Banner, M. L., Barthelmy, X., and Allis, M. J., "On the threshold for wave breaking of two-dimensional deep water wave groups in the absence and presence of wind," *J. Fluid Mech.* **811**, 642–658 (2017).
- Sethian, J. A., and P. Smereka, "Level set methods for fluid interfaces," *Annu. Rev. Fluid Mech.* **35**, 341–372 (2003).
- Smagorinsky, J., "General circulation experiments with the primitive equations: I. The basic experiment," *Mon. Weather Rev.* **91**(3), 99–164 (1963).
- Sous, D., Forsberg, P. L., Touboul, J., and Nogueira, G. G., "Laboratory experiments of surf zone dynamics under on- and offshore wind conditions," *Coastal Eng.* **163**, 103797 (2021).
- Stansell, P., Wolfram, J., and Zachary, S., "Horizontal asymmetry and steepness distributions for wind-driven ocean waves from severe storms," *Appl. Ocean Res.* **25**(3), 137–155 (2003).
- Sullivan, P. P., Banner, M. L., Morison, R. P., and Peirson, W. L., "Turbulent flow over steep steady and unsteady waves under strong wind forcing," *J. Phys. Oceanography* **48**(1), 3–27 (2018).
- Sussman, M., "A second order coupled level set and volume-of-fluid method for computing growth and collapse of vapor bubbles," *Journal of Computational Physics* **187**(1), 110–136 (2003).
- Tian, Z., and Choi, W., "Evolution of deep-water waves under wind forcing and wave breaking effects: Numerical simulations and experimental assessment," *Eur. J. Mech. B Fluids* **41**, 11–22 (2013).
- Tian, Z., Perlin, M., and Choi, W., "An eddy viscosity model for two-dimensional breaking waves and its validation with laboratory experiments," *Phys. Fluids* **24**(3), 036601 (2012).
- Touboul, J., Giovanangeli, J. P., Kharif, C., and Pelinovsky, E., "Freak waves under the action of wind: Experiments and simulations," *Eur. J. Mech. B Fluids* **25**(5), 662–676 (2006).
- Vukčević, V., Jasak, H., and Gatin, I., "Implementation of the Ghost Fluid Method for free surface flows in polyhedral Finite Volume framework," *Computers fluids* **153**, 1–19 (2017).
- Weller, H. G., "Derivation, modelling, and solution of the conditionally averaged two-phase flow equations," Technical Report No. TR/HGW/02 (OpenCFD Ltd., 2005).
- Wu, C. H., and Yao, A., "Laboratory measurements of limiting freak waves on currents," *J. Geophys. Res. Oceans* **109**(C12), C12002, <https://doi.org/10.1029/2004JC002612> (2004).
- Wu, J., "Wind-induced drift currents," *J. Fluid Mech.* **68**(01), 49–70 (1975).
- Wang, Z., Q.-P. Zou, and D. Reeve, "Simulation of spilling breaking waves using a two phase flow CFD model," *Comput. Fluids* **38**, 1995–2005 (2009).
- Xie, Z., "Numerical modelling of wind effects on breaking solitary waves," *Eur. J. Mech. B Fluids* **43**, 135–147 (2014).
- Xie, Z., "Numerical modelling of wind effects on breaking waves in the surf zone," *Ocean Dyn.* **67**(10), 1251–1261 (2017).
- Xie, Z., and Lin, P., "Eulerian and Lagrangian transport by shallow-water breaking waves," *Phys. Fluids* **34**(3), 032116 (2022).
- Yan, S., and Ma, Q. W., "Numerical simulation of wind effects on breaking solitary waves," in *The Nineteenth International Offshore and Polar Engineering Conference*, Osaka, Japan, 21–26 July, 2009.
- Yan, S., and Ma, Q. W., "Numerical simulation of interaction between wind and 2D freak waves," *Eur. J. Mech. B Fluids* **29**(1), 18–31 (2010).
- Yan, S., and Ma, Q. W., "Improved model for air pressure due to wind on 2D freak waves in finite depth," *Eur. J. Mech. B Fluids* **30**(1), 1–11 (2011).
- Yao, A., and Wu, C. H., "Incipient breaking of unsteady waves on sheared currents," *Phys. Fluids* **17**, 082104 (2005).
- Yao, A., and Wu, C. H., "Spatial and temporal characteristics of transient extreme wave profiles on depth-varying currents," *J. Eng. Mech.* **132**, 1015–1025 (2006).

- Zhang, Y., Q.-P. Zou, and D. Greaves, “Numerical simulation of free-surface flow using the level-set method with global mass correction,” *Int. J. Numer. Methods Fluids* **63**, 651–680 (2010).
- Zou, Q., and Chen, H., “Wind and current effects on extreme wave formation and breaking,” *J. Phys. Oceanogr.* **47**(7), 1817–1841 (2017).
- Zou, Q., and Peng, Z., “Evolution of wave shape over a low-crested structure,” *Coastal Eng.* **58**(6), 478–488 (2011).
- Zdyrski, T., and Feddersen, F., “Wind-induced changes to surface gravity wave shape in deep to intermediate water,” *J. Fluid Mech.* **903**, A31 (2020).
- Zdyrski, T., and Feddersen, F., “Wind-induced changes to surface gravity wave shape in shallow water,” *J. Fluid Mech.* **913**, A27 (2021).
- Zdyrski, T., and Feddersen, F., “Wind-induced changes to shoaling surface gravity wave shape,” *Physical Review Fluids* **7**(7), 074802 (2022).